Materials Advances

ROYAL SOCIETY OF CHEMISTRY

PAPER

View Article Online
View Journal

Cite this: DOI: 10.1039/d5ma01318f

Rigidifying donor–acceptor frameworks *via* C–C interlocking to modulate excited-state dynamics in HLCT emitters

L. N. S. Laya Pagadala, [a] Sivakumar Vaidyanathan [b] and Mahesh Kumar Ravva *[ac]

Received 13th November 2025,
Accepted 12th March 2026

DOI: 10.1039/d5ma01318f

rsc.li/materials-advances

Thermally activated delayed fluorescence (TADF) exploits intramolecular charge-transfer states to harvest triplet excitons in organic light-emitting diodes (OLEDs) through the twisted configuration of the donor and acceptor units. However, the highly twisted conformation of TADF molecules results in limited fluorescence yield and leads to energy loss. In this study, we designed rigid and planar fused HLCT emitters by interlocking the C–C bond between the donor and the acceptor. Carbazole and π-extended carbazole derivatives were used as donors, and cyano benzene, benzophenone, sulfonyldibenzene, and *N*-methyl phthalimide were employed as acceptors. Density functional theory (DFT) and time-dependent density functional theory (TD-DFT) were used to evaluate the electronic, excited-state, and photophysical properties of the newly designed molecules. The radiative and non-radiative decay rates were estimated using the thermal vibrational correlated formalism (TVCF). Furthermore, the light emitting properties of organic emitters with and without interlocked structures were systematically evaluated. These results reveal the crucial role of molecular rigidity in enhancing radiative and non-radiative properties of organic emitters. Overall, our findings establish intricate relationships between the molecular structure and key photochemical properties, including intersystem crossing rates, reverse intersystem crossing rates, radiative decay rates, and charge transfer characteristics.

1. Introduction

Thermally activated delayed fluorescence (TADF) is a mechanism by which triplet electrons can be harvested to generate fluorescence, and is used in organic light-emitting diodes (OLEDs), which enables high efficiency without the involvement of noble metals.[1,2] In optoelectronic devices, these TADF emitters play a critical role in ultrapure luminescence, providing a wide colour gamut. The advantage of TADF emitters is their capability to utilize both singlet and triplet excitons, enabling 100% internal quantum efficiency (IQE) in OLEDs.[3,4] Compared with traditional fluorescence (first-generation OLEDs) and phosphorescence (second-generation OLEDs), researchers have focused on enhancing the device efficiency and colour purity by establishing TADF emitters (third-generation OLEDs).[5,6]

The main factor in the TADF mechanism is the maintenance of a smaller energy gap between the singlet and triplet excited states (ΔE_{ST}) and spin–orbit coupling (SOC), which facilitates faster reverse intersystem crossing (RISC).[7,8] These factors depend on the structure of the molecule (twisted donor and acceptor), which can promote spatial separation between the highest occupied molecular orbital (HOMO) and the lower unoccupied molecular orbital (LUMO). The separation between the HOMO and LUMO wavefunctions depends on the dihedral angle between the donor and acceptor units.[9] The larger dihedral angles between the donor and acceptor units effectively separated the HOMO and LUMO distributions, resulting in smaller ΔE_{ST} values. These reduced energy gaps enable efficient harvesting of triplet excitons through the RISC process.[10] Three mechanisms have been proposed for conversion of triplet excitons to singlet excitons to realize a theoretical internal quantum efficiency (IQE) of 100%: triplet–triplet annihilation (TTA),[11,12] TADF and hybrid local and charge transfer (HLCT) emission.[13,14]

To enhance the TADF properties, researchers have explored replacing planar acceptors with non-planar acceptors to increase the twist angle.[15] Various molecular architectures have

[a] *Department of Chemistry, SRM University-AP, Amaravati, 522240, India. E-mail: mahesh.r@srmap.edu.in*
[b] *Department of Chemistry, Indian Institute of Technology Hyderabad, Kandi, Sangareddy, 502285, India*
[c] *Centre for Computational and Integrative Sciences, SRM University-AP, Amaravati, 522240, India*

been developed to achieve smaller singlet–triplet energy gaps, including donor–acceptor (D–A) systems with spiro-linkages[16] and through-space charge transfer (TSCT)[17] configurations that optimize the spatial arrangement of the donor and acceptor units. However, the lack of interlocking between the donor and acceptor units induces structural relaxation in TADF emitters and leads to an increased Stokes shift and broadened emission spectra.[18,19] Typical TADF emitters exhibit the emission spectra with a full-width at half-maximum (FWHM) of approximately 100 nm.[20–23] OLED displays incorporate color filters or optical microcavities to meet the broadcasting standards of color purity by trimming the broad emission tail.[24] However, this approach leads to efficiency loss, which makes it challenging to realize high efficiency OLED displays with the existing TADF emitters.[25–27]

It has been shown that RISC exists from high-lying triplet states (hRISC, T_n, $n \geq 2$) in organic emitters.[13,14] The molecules exhibiting hRISC up-conversion are referred to as HLCT molecules. In order to achieve high color purity, it is important to develop molecular design strategies that can effectively narrow the FWHM of emission in HLCT emitters with D–A structures.[28] The traditional HLCT emitters contain large twist between the donor and acceptor units, which facilitates spatially separated HOMO–LUMO. During the excitation process, such separation promotes the charge-transfer (CT) character but also enables facile torsional motion between the donor and acceptor units. It is important to understand whether broad emission originates from the CT process, structural relaxations, or their combined effects.[29] It has been shown that the large dihedral angles introduced in typical D–A configurations facilitate twisted intramolecular charge transfer (TICT).[28]

Through bond charge transfer (TBCT) and TICT are emerging as common design strategies to enhance the TADF properties. However, TBCT has gained much attention compared to TICT to regulate excited-state properties in D–A systems. In TBCT systems, donor and acceptor units are electronically coupled through a π-conjugated backbone rather than a twisted configuration. Such bonding interactions enable controlled delocalization of Frontier molecular orbitals while maintaining structural rigidity. Compared to TICT-based emitters, C–C interlocking along with TBCT systems can suppress excessive structural relaxation and reduce emission broadening while still maintaining a small ΔE_{ST}.[30–32] The balance between orbital overlap and spatial separation in TBCT architectures provides an effective pathway to achieve fast RISC with improved colour purity. Therefore, incorporating through-bond interactions in rigid D–A frameworks represents a promising strategy to overcome the limitations of conventional twisted architectures.[33,34]

Recently, multiple resonance MR-TADF emitters have been developed with extremely narrow FWHM.[35] Typically, MR-TADF emitters exhibit a slower rate of reverse intersystem crossing. Various strategies such as integration of heavy atoms into the core, π-conjugation extension, and peripheral substitution of various donor and acceptor units are used to improve the rate of reverse intersystem crossing.[36] In general, these strategies are limited to MR-TADF materials and aren't applicable to traditional D–A architecture HLCT emitters. Therefore, it is important to develop design strategies to achieve faster RISC and decrease the emission FWHM of HLCT emitters with D–A architectures. Recently, Chan *et al.* proposed a D–A-based deep-blue emitter which contains a 3,6-substituted carbazole as the donor and benzonitrile as the acceptor.[37] These authors have shown that a reduced FWHM from 79 nm to 55 nm in obtained through functional group modification. However these emitters suffer from a low external quantum efficiency.[37] To address these challenges, emitters with a lower FWHM and higher external quantum efficiency are essential.

Recently, Patil *et al.* proposed a new design strategy involving the interlocking of carbazole and benzene in *N*-phenyl carbazole (indolo[3,2,1-*jk*] carbazole (ICz)). The ICz motif has a more planar structure than triphenyl amine and *N*-phenyl carbazole.[38] Compared with state-of-the-art narrow-emitting boron–nitrogen-type materials, ICz-based TADF emitters exhibit an exceptionally narrow FWHM (below 20 nm) along with

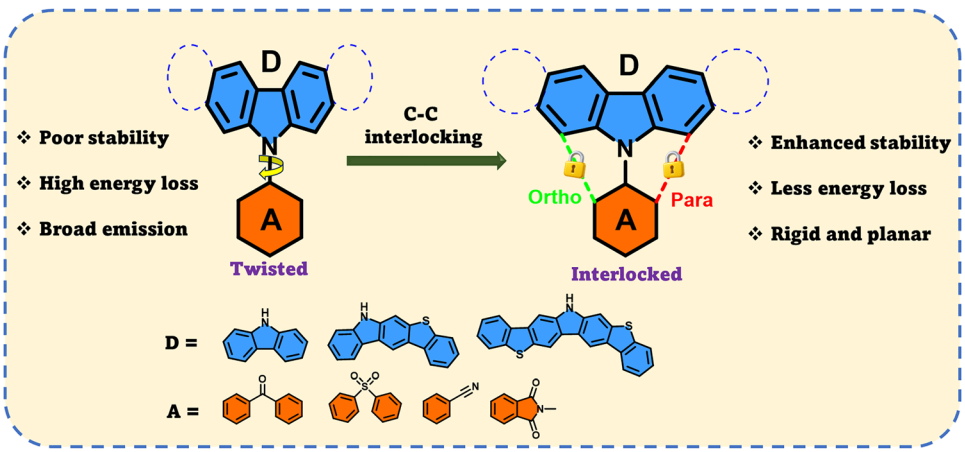

Scheme 1 Schematic representation of the molecular design of the *ortho*- and *para*-configured donor–acceptor HLCT emitters considered in this study.

high color purity and an external quantum efficiency above 30%. The planar and rigid nitrogen-centered tripod structure of ICz has extended π-electron conjugation and delocalization of non-bonding electrons over three benzene rings.[39] As reported previously, this building block possesses unique characteristics, such as charge transport and emission properties due to its deeper HOMO and LUMO compared to the other indolocarbazole derivatives.[38,40]

Inspired by this design principle, our research work explores an unconventional approach to develop a rigid, planar D–A-type emitter through C–C interlocking at the *ortho*- and *para* positions between the donor and acceptor fragments (Scheme 1). By systematically modifying the strength of the donor and acceptor units, we investigated how structural rigidity influences intersystem crossing, and reverse intersystem crossing, radiative emission, and non-radiative emission using density functional theory methods. Furthermore, comparative analysis between rigid and non-rigid systems, an aspect not reported previously, reveals that the interlocking between the donor and acceptor fragments effectively suppresses the non-radiative decay. The non-rigid analogues show higher non-radiative decay through structural relaxation leading to poor quantum yield.

2. Molecular design strategy

In this study, we developed a series of novel rigid π-conjugated and planar donor (D)–acceptor (A)-type molecules by interlinking the carbon-3 (C3) and carbon-12 (C12) positions of the carbazole (CZ) unit, referred to as the *ortho* (O) and *para* (P) configurations (Scheme 1). Our analysis revealed that the electronic properties of these newly designed *ortho*- and *para*-substituted molecules can aid in the development of OLED materials using the ''rigid π-conjugated and planar'' approach. Carbazole (CZ), carbazole fused with one benzothiophene group (B1Cz), and carbazole fused with two benzothiophene groups (B2Cz) were selected as the donor units because of their electron-donating ability and electron-withdrawing groups such as cyano benzene, benzophenone, diphenyl sulfide, and

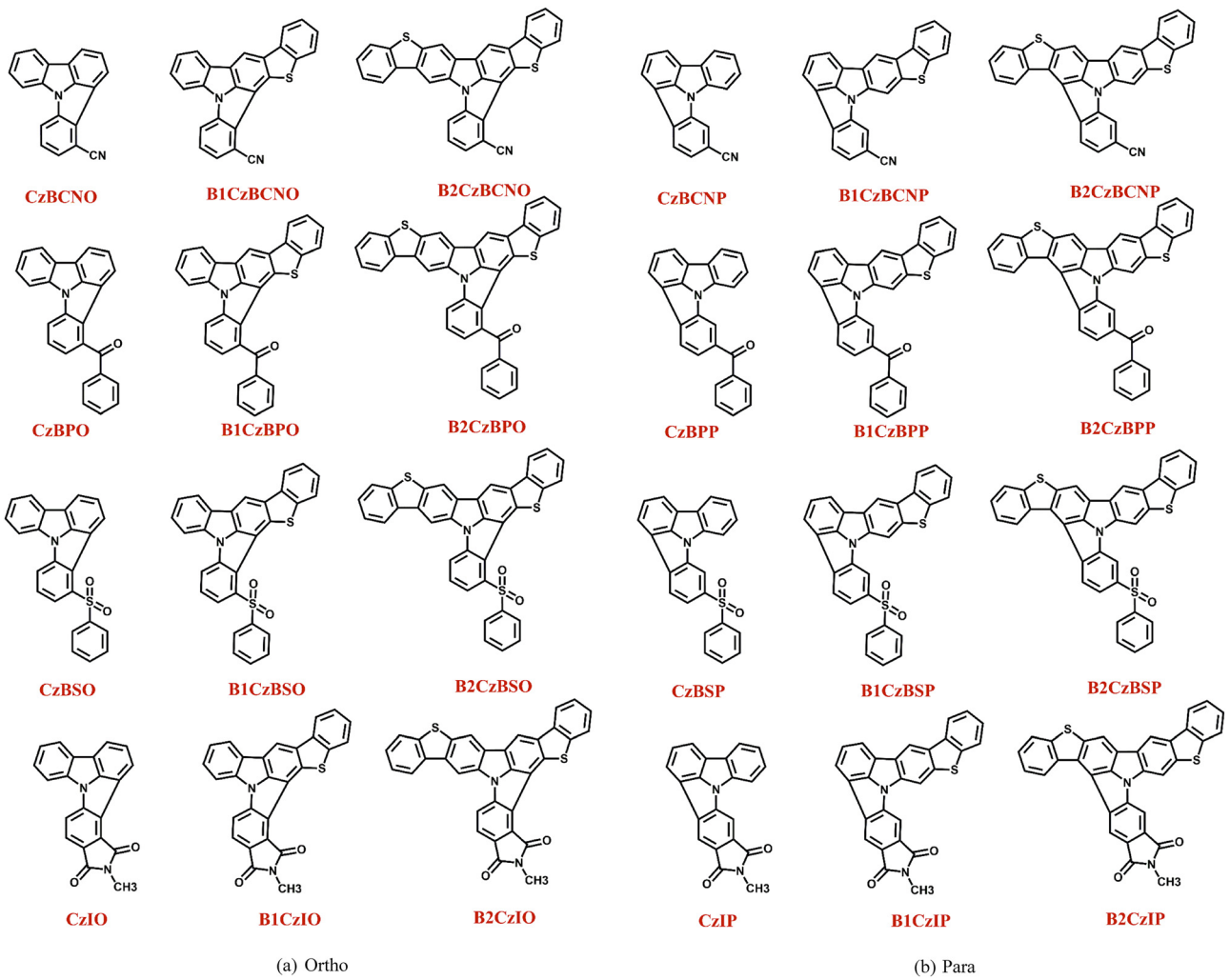

Fig. 1 Chemical structures of (a) *ortho* and (b) *para* substituted designed molecules.

n-methyl phthalimide. A total of 24 π-conjugated rigid donor (D)–acceptor (A) substructure *ortho*- and *para*-substituted molecules were designed by combining the aforementioned *ortho* and *para* donor–acceptor fragments, as shown in Fig. S1.

3. Computational methodology

The ground-state (S_0) geometries were optimized using density functional theory (DFT) with the PBE0[41] functional and the 6-31G(d,p)[42] basis set. The five lowest excited singlet states and the triplet states were computed using TD-DFT[43] with the same functional and basis set. Natural transition orbital (NTO)[44] analysis was performed to characterize the nature of the excited states. Benchmark calculations were carried out to assess the performance of different hybrid and range-separated functionals (B3LYP, PBE0, BMK, M06-2X, ωB97XD, and CAM-B3LYP). The calculated values are listed in Table S1. Among the functionals considered, the values obtained using PBE0 are in good agreement with the experimental values. The PBE0 hybrid density functional was found to be particularly effective for modelling charge-transfer excitations.[45] All calculations for both the ground and excited states were performed using the Gaussian 16 software.[46] In addition, the charge transfer values were determined using the Multiwfn code. The spin–orbit coupling (SOC) values were computed *via* TD-DFT calculations using the PBE0 functional and DEF2-TZVP as the basis set in the ORCA[47] software package. The RISC rates were derived from the classical Marcus rate equation,[48] and both the RISC and ISC rates were estimated using the Fortran code.

4. Results and discussion

4.1. Ground-state geometries

Fig. 1 shows the chemical structures of the designed *ortho*- and *para*-interlocked HLCT emitters. In these systems, the covalent bond between the C3/C12 positions of carbazole and the *ortho*/*para* positions of the benzene ring results in a planar conformation of the *N*-substituted benzo carbazole unit. Such planarity can enhance π-electron delocalization between the carbazole and benzene rings. However, benzophenone and diphenyl sulphide-substituted molecules (**CzBPO**, **B1CzBPO**, **B2CzBPO**, **CzBSO**, **B1CzBSO**, **B2CzBSO**, **CzBPP**, **B1CzBPP**, **B2CzBPP**, **CzBSP**, **B1CzBSP**, and **B2CzBSP**) exhibit a slight twist in their geometry due to steric hindrance between hydrogen atoms of the phenyl rings. The calculated dihedral angles between the two benzene units for both the *ortho*- and *para*-substituted molecules are listed in Table S2. It is interesting note that in the cases of **CzBPO**, **B1CzBPO**, and **B2CzBPO**, the calculated twist angle values are 29°, 22°, and 22°, respectively. In the case of **B1CzBPO** and **B2CzBPO**, the interaction between the oxygen atom of the ketone group and the sulphur atom of the thiophene unit alters the twist angle between the phenyl rings. A similar phenomenon is observed for **B1CzBSO** and **B2CzBSO**. However, no change in the twist angle is observed for

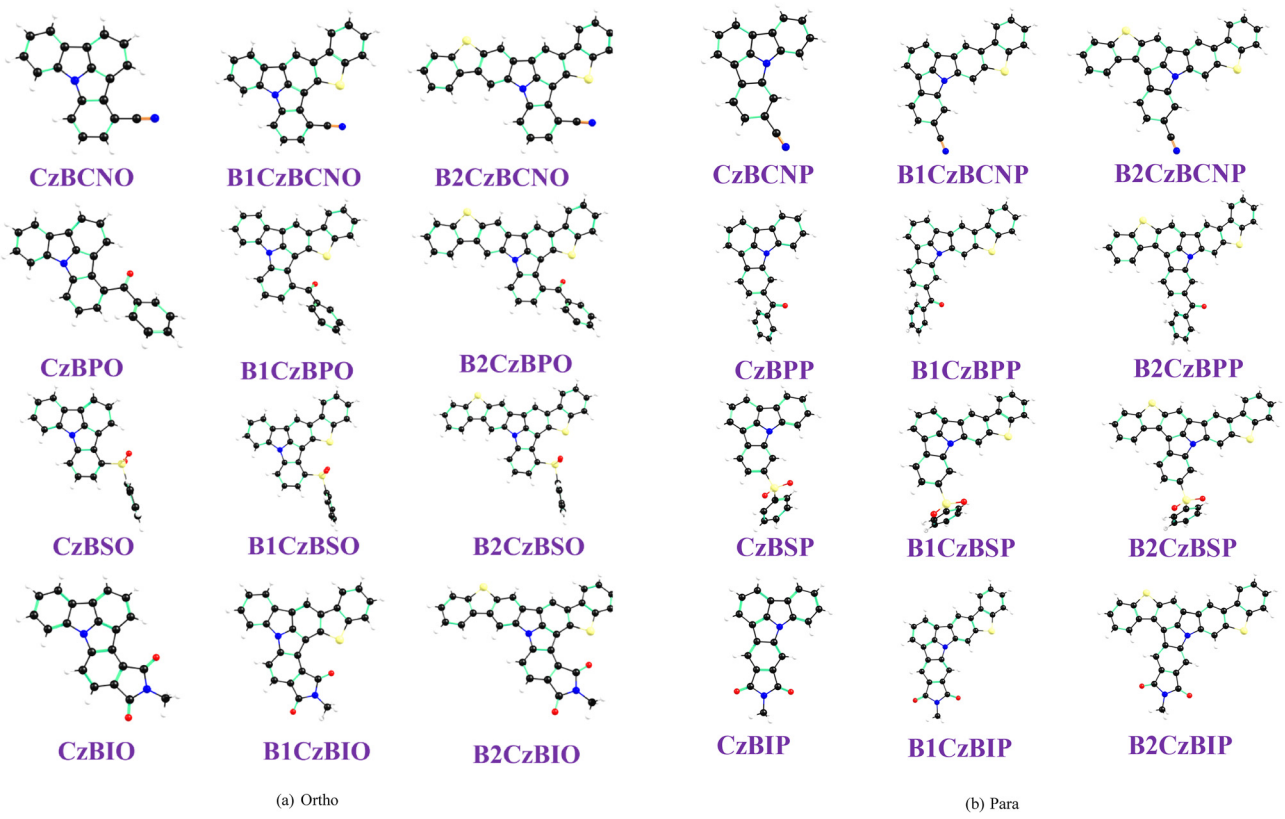

Fig. 2 Optimized π-conjugated rigid (a) *ortho*- and (b) *para*-configured molecules obtained at the PBE0/6-31G(d,p) level of theory.

para-interlocked molecules, such as **B1CzBPP** and **B2CzBPP**, owing to the absence of S···O interactions. All ground state optimized geometries are depicted in Fig. 2.

4.2. Frontier molecular orbital (FMO) analysis

The electronic structures of the designed molecules were analysed using the highest occupied molecular orbital (HOMO) and the lowest unoccupied molecular orbital (LUMO). Fig. S1 shows the electron density distributions of the HOMO and the LUMO across the donor and acceptor units in the *ortho*- and *para*-substituted molecules. The HOMO was primarily localized on the electron-donating CZ, B1Cz, and B2Cz units in the CZ derivatives and extended to the adjacent benzene ring. The LUMO is mainly localized in the electron-acceptor region, with a slight extension to the benzene ring due to π-conjugation between the donor and acceptor moieties. The HOMO energy values became less negative with an increasing number of donor units from Cz to B2Cz with all different acceptors in both *ortho*- and *para*-interlocked molecules (Fig. 3(a) and (b) and Table S3). The LUMO energy values varied in the following order: *N*-methyl phthalimide > benzophenone > cyanobenzene > diphenyl sulfide. As described previously, the presence of S···O interactions alters the twist angle between the phenyl rings in the acceptor group in the B1Cz and B2Cz substituted molecules. Consequently, different trends were observed in the LUMO energies. Notably, this trend shifted in the presence of stronger donor units, such as B1Cz and B2Cz, with the LUMO stabilization sequence: *N*-methyl phthalimide > cyano benzene > benzophenone > sulfonyl dibenzene (Fig. 3(b)).

Additionally, a comparison between *ortho*- and *para*-interlocked systems revealed that *para*-interlocked molecules generally exhibited slightly higher LUMO energy values. From these observations, it can be concluded that *N*-methyl phthalimide acts as a strong electron acceptor, whereas dibenzothiophene–carbazole (B2Cz) serves as a strong donor among the studied systems. The donor–acceptor pairing follows the order of effectiveness: **B2CzIO** > **B1CzIO** > **CzIO** in both the *ortho* and *para* configurations. This trend is rationalized by the capacity of the strong electron-donating and electron-withdrawing groups to induce a favourable spatial overlap between the HOMO and the LUMO, facilitating intramolecular charge transfer, although it has a rigid and planar structure.

4.3. Excited state characteristics

The calculated absorption energies for **CzIO** and **CzIP** are 380 and 370 nm, respectively (Table 1). These values are in good agreement with the experimental values;[49] however, systems incorporating strong electron-withdrawing groups (*e.g.*, cyanobenzene and phthalimide) in conjunction with strong electron-donating units (*e.g.*, bis-benzothiophene) show distinct absorption properties extending into the visible region (listed in Table 1). This effect is attributed to enhanced π-electron delocalization between the donor and acceptor segments, which promotes a more rigid and planar molecular conformation, thereby facilitating lower-energy electronic transitions.

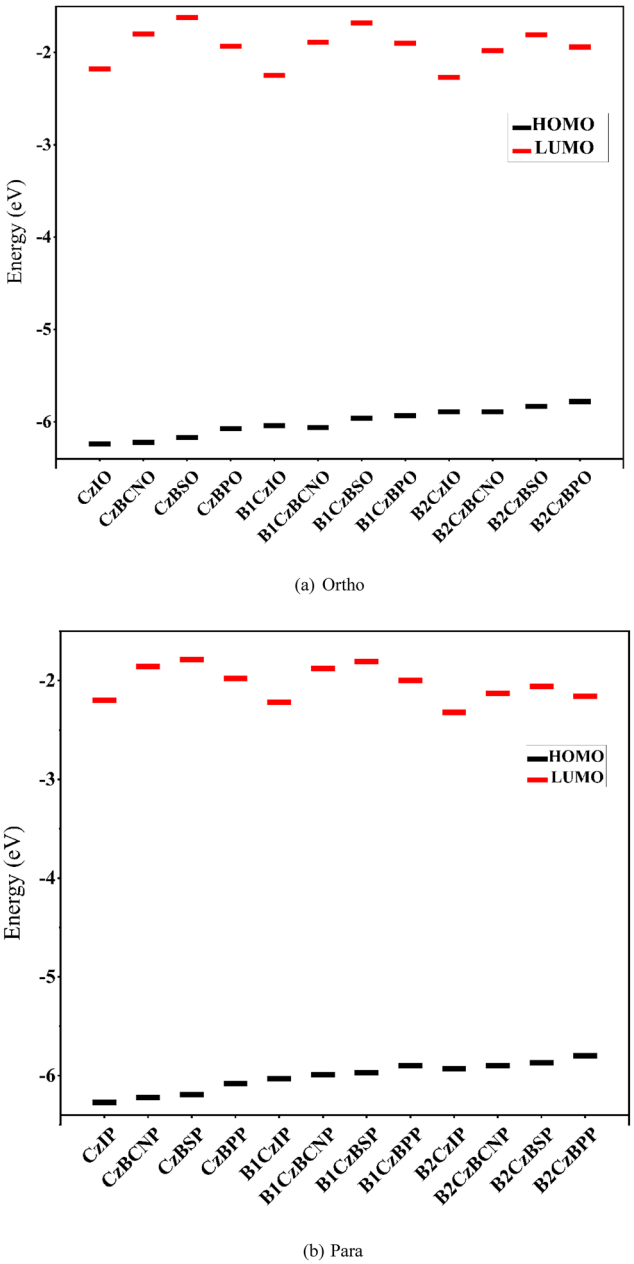

Fig. 3 FMO analysis for the designed (a) *ortho* and (b) *para* interlocked molecules obtained at the PBE0/6-31G(d,p) level of theory.

Among all *ortho*-substituted molecules, **B2CzIO** showed the lowest absorption energy value (2.95 eV). The strong electron-donating (benzothiophene) and electron-withdrawing (phthalimide) natures led to the lowest absorption energies compared to the other substituents. For *para*-interlocked molecules, **B2CzBCNP** exhibited the lowest absorption energy (S_1) of 2.90 eV. Overall, all the designed molecules exhibited absorption energies in the range of 2.90 to 3.71 eV. The marginal difference between the absorption energies of the *ortho*- and *para*-interlocked molecules reveals that both have similar π-electron delocalization. From Cz to B2Cz, the strength of the donor increases and the value of the excitation energy decreases.

Table 1 Singlet and triplet excited state energies of *ortho* and *para* interlocked molecules determined at the TD-PBE0/6-31G(d,p) level of theory

Molecules	S_1 (eV)	T_1 (eV)	T_2 (eV)	T_3 (eV)	T_4 (eV)	T_5 (eV)
CzBCNO	3.61	2.80	2.94	3.24	3.48	3.83
CzBPO	3.41	2.76	2.88	3.05	3.18	3.38
CzBSO	3.71	2.86	3.08	3.27	3.58	3.65
CzIO	3.27	2.66	2.85	3.20	3.25	3.48
B1CzBCNO	3.42	2.58	2.83	3.21	3.23	3.39
B1CzBPO	3.33	2.63	2.87	3.08	3.20	3.24
B1CzBSO	3.54	2.66	2.95	3.26	3.29	3.59
B1CzIO	3.07	2.50	2.67	3.03	3.08	3.23
B2CzBCNO	3.22	2.51	2.69	2.97	3.19	3.27
B2CzBPO	3.18	2.54	2.72	2.96	3.07	3.18
B2CzBSO	3.31	2.54	2.81	3.00	3.27	3.33
B2CzIO	2.95	2.46	2.53	2.92	2.94	3.11
CzBCNP	3.56	2.78	3.01	3.06	3.77	3.85
CzBPP	3.36	2.72	2.90	3.01	3.14	3.41
CzBSP	3.61	2.85	3.08	3.13	3.57	3.78
CzIP	3.35	2.68	2.87	2.98	3.54	3.62
B1zBCNP	3.40	2.71	2.88	2.97	3.24	3.49
B1CzBPP	3.23	2.69	2.80	2.89	3.11	3.22
B1CzBSP	3.45	2.74	2.96	3.03	3.29	3.50
B1CzIP	3.18	2.64	2.73	2.90	3.19	3.36
B2CzBCNP	2.90	2.28	2.36	2.79	3.03	3.22
B2CzBPP	3.10	2.44	2.52	2.84	3.05	3.35
B2CzBSP	3.14	2.47	2.63	2.91	3.15	3.39
B2CzIP	3.00	2.42	2.56	2.70	3.11	3.24

To gain deeper insights into the ''π-conjugated rigid'' molecules, we need to explore the characteristics of the excited states, energy level alignments, and transition properties. A natural transition orbital (NTO) analysis was performed to understand and characterize the nature of the excited state. NTOs offer a clear representation of electronic excitations, characterizing the relevant excited states as a pair of orbitals that represent the hole and electron wave functions. The NTOs of the designed molecules are shown in Fig. S2. Based on the delocalization of the hole and electron wavefunctions, the excitation can be classified into local excitation (LE), charge transfer (CT), and hybridized local and charge transfer (HLCT). LE occurs when holes and electrons overlap within the same spatial region. CT occurs when there is a significant spatial separation between the hole and electron, leading to a noticeable shift in the charge density. HLCT refers to an excited state in which both LE and CT characteristics co-exist.[50,51] In addition, the nature of an excited state can be qualitatively described by hole and electron wavefunctions (as represented by NTOs). In addition, the Δr index, which represents the distance between the hole and the electron, can quantitatively characterize the nature of the excited states. The calculated Δr indices of the designed *ortho*- and *para*-substituted molecules are listed in Table S4. By examining the delocalization of the hole and electron wavefunctions (Fig. S2) and Δr index values (Table S4), one can determine whether the excitation was LE, CT, or HLCT. In the LE state, the hole and electron wave functions overlap significantly and the Δr value is small. In the CT state, holes and electrons are spatially separated in different regions of the molecule, resulting in larger Δr values. As mentioned earlier, HLCT is a hybrid state with the features of both CT and LE. Unlike the LE and CT states, the hole and electron wavefunctions in HLCT exhibit partial overlap rather than complete separation (as in CT) or strong overlap (as in LE). From the above information, we observed that both benzophenone and phthalimide acceptor units have higher Δr values (>3 Å) with Cz, B1Cz, and B2Cz donors. This clearly reveals that the centroids of both the hole and electron wavefunctions are separated in the aforementioned molecules. In contrast, sulfonyldibenzene and cyanobenzene acceptor units show lower Δr values (<3 Å) with three donor units in the *ortho*-substituted molecules. We found that the Δr values depend on the strength of the acceptor units. Molecules with stronger acceptor units, such as I and BP units, exhibit a large distance between the hole and electron wavefunctions. Visual inspection of the hole and electron wavefunction delocalization and moderate values of the Δr index reveal that the nature of the excited state in these molecules is HLCT, as overlap in the hole and electron wavefunctions is observed. Overall, all designed molecules showed either HLCT- or LE-dominated HLCT properties in the lowest S_1 state.

4.4. Photophysical properties

Thus, a rapid reverse intersystem crossing (RISC) from the lower triplet excited states (T_m) to the lowest singlet excited states (S_1) can be obtained according to the classical Marcus eqn (1)[48]

$$k = \frac{2\pi}{\hbar}|H_{SOC}|^2 \frac{1}{\sqrt{4\pi\lambda k_B T}} \exp\left(\frac{-\left(\lambda + \Delta E_{S_1T_m}\right)^2}{4\lambda k_B T}\right) \quad (1)$$

where k is the rate of RISC, $|H_{SOC}|$ is the spin–orbit coupling between the initial (triplet) and final (S_1) states, λ is the reorganization energy (both inner and outer spheres, considered as 0.1 eV in this study), and $\Delta E_{S_1T_m}$ is the energy gap between the S_1 and T_m states, k_B is the Boltzmann constant, and T is 298 K.

We observed that the calculated $\Delta E_{S_1T_m}$ values for all designed molecules are less than 0.2 eV, except **B1CzBSO**, **CzBCNP**, **CzIP**, **B1CzIP**, **B2CzBSP**, and **B2CzIP**. For efficient exciton utilization efficiency (EUE), the gap between the lowest singlet state (S_1) and the nearest triplet state (T_m) should be less than 0.2 eV.[48,52] It is important to note that, in traditional HLCT emitters, the donor and acceptor units are separated by twist angle to spatially separate the HOMO and the LUMO. As discussed previously, such a spatial separation leads to a smaller energy gap between the singlet and triplet states. In our designed molecules, even though the donor and acceptor molecules exhibit a planar conformation, they exhibit smaller $\Delta E_{S_1T_m}$ values. This enables an efficient RISC process, even for the planar confirmation of the HLCT emitters.

Another important factor that plays a crucial role in the EUE process is spin–orbit coupling (SOC). We have calculated the SOC between S_1 and the lowest five triplet states (T_1–T_5) and the same values are depicted in Fig. 4. Among all the designed molecules, the **CzBPO** molecule showed a higher SOC value (3.75 cm^{-1}). The SOC value depends on the presence of

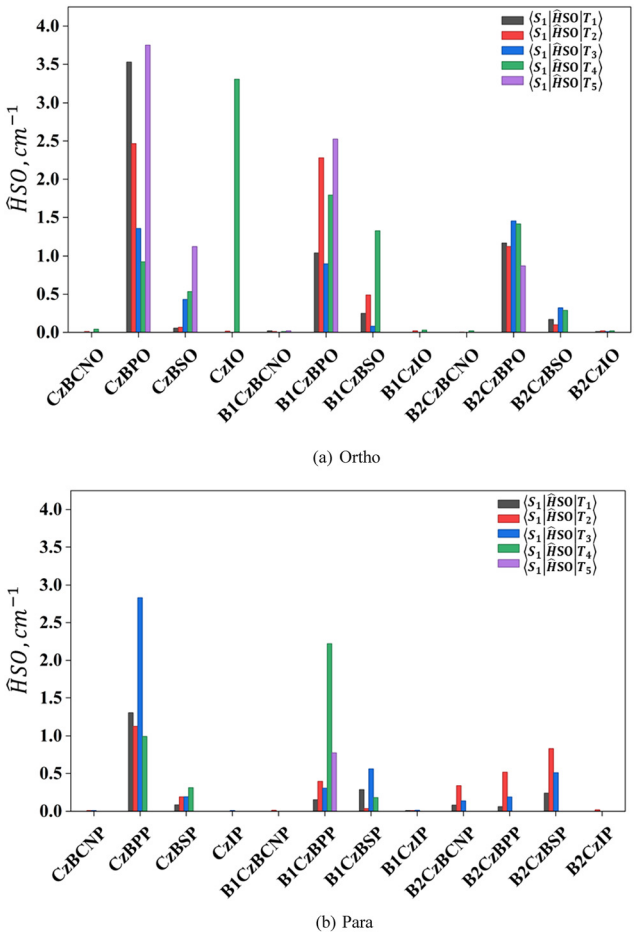

Fig. 4 Calculated SOC between S_1 and the lowest five triplet states (T_1–T_5) for designed (a) *ortho* and (b) *para* interlocked molecules obtained at the PBE0/DEF2-TZVP level of theory.

heteroatoms, such as N, O, and S. According to El-Sayed's rule, stronger SOC for transitions involves a change in orbital type. Thus, the S_1 state with CT character and higher-lying triplet state (T_m) with LE character exhibit stronger SOC values. In the cases of **CzBPO**, **CzIO**, **B1CzBPO**, and **B2CzBPP**, we have observed stronger SOC values (Table 2 and Fig. S3).

The calculated ISC and RISC rates for all molecules are listed in Table 2. Among all designed molecules, **CzBPO**, **CzIO**, **B1CzBPO**, **B2CzBPO** and **B1CzBPP** have shown higher RISC values ($>10^7$ S^{-1}).

5. Fluorescence efficiency

5.1. Rate of radiative emission (k_r)

Traditional HLCT emitters have twisted dihedral angles between the donor and acceptor units. As a result, the excited state in the lowest S_1 state is generally CT in nature. The HLCT emitters, which have CT dominated character in the S_1 state, exhibit a reduced rate of radiative emission (fluorescence) due to the spatial separation between the HOMO and LUMO distributions on the donor and acceptor.

Table 2 Calculated SOC (cm^{-1}), RISC (S^{-1}), and ISC (S^{-1}) values for the designed molecules

Molecules	$\Delta E_{S_1T_m}$ (eV)	SOC (cm^{-1})	k_{ISC} (s^{-1})	k_{RISC} (s^{-1})
CzBCNO	0.13	0.04	1.10×10^6	7.50×10^3
CzBPO	0.03	3.75	7.10×10^9	2.20×10^9
CzBSO	0.06	1.12	8.70×10^8	8.40×10^7
CzIO	0.02	3.31	4.70×10^9	2.20×10^9
B1CzBCNO	0.03	0.02	2.00×10^5	6.30×10^4
B1CzBPO	0.09	2.52	5.10×10^9	1.50×10^8
B1CzBSO	0.25	1.33	3.60×10^4	9.60×10^3
B1CzIO	0.04	0.00	0	0
B2CZBCNO	0.02	0.02	1.70×10^5	1.70×10^5
B2CzBPO	0.00	0.86	2.20×10^8	2.20×10^8
B2CzBSO	0.04	0.29	4.80×10^7	1.00×10^7
B2CzIO	0.01	0.02	1.40×10^5	1.00×10^5
CzBCNP	0.50	0.01	1.40×10^{-2}	5.00×10^{-11}
CzBPP	0.21	0.99	2.40×10^8	6.90×10^4
CzBSP	0.05	0.31	6.10×10^7	8.70×10^6
CzIP	0.37	0.01	6.70×10^1	3.70×10^{-5}
B1zBCNP	0.15	0.00	0	0
B1CzBPP	0.01	0.77	2.10×10^8	1.40×10^8
B1CzBSP	0.16	0.18	5.70×10^4	3.60×10^4
B1CzIP	0.28	0.01	3.40×10^3	6.40×10^{-4}
B2CZBCNP	0.11	0.14	7.20×10^6	2.10×10^5
B2CzBPP	0.05	2.09	2.70×10^9	3.90×10^8
B2CzBSP	0.23	0.51	4.00×10^7	5.30×10^3
B2CzIP	0.30	0.17	4.80×10^5	4.4

In the case of our newly designed molecules, as described earlier, most of the molecules exhibited LE dominated HLCT characteristics in the S_1 state. Consequently, the oscillator strength of the designed molecules is higher, which leads to an increase in the radiative emission rate (fluorescence) because of the improved HOMO and LUMO overlap between the donor and acceptor. According to Einstein's spontaneous eqn (2), the radiative emission is directly proportional to the oscillator strength and vertical emission energy:

$$k_r = \frac{f\Delta E_{fi}{}^2}{1.499} \quad (2)$$

where f is the oscillatory strength and ΔE_{fi} is the vertical emission energy. The calculated oscillator strengths, vertical emission energies, and rates of radiative emission are shown in Fig. 5. All the designed molecules' oscillator strengths range from 0.01 to 0.80. It can be seen from Fig. 5 that Cz-based molecules show emission in the 2.77–3.30 eV range (blue region). The introduction of B1 and B2 units onto the Cz stabilized the excited states and shifted the emission down to 2.48 to 3.10 eV. Among all the designed molecules, **B2CzBSO** has the highest oscillator strength (f) value. The calculated radiative rates for all the molecules ranged from 10^6 to 10^8 s^{-1}. The Cz-based molecules showed moderate values ($\sim 10^7$ s^{-1}), whereas the introduction of B1 and B2 units, particularly in combination with the sulfonyl dibenzene acceptor (**B1CzBSO**, **B2CzBSO**, and **B2CzBSP**), dramatically enhanced the radiative emission ($>10^7$ s^{-1}). The phthalimide-containing molecules **CzIO**, **B1CzIO**, and **B2CzIO** showed inefficient radiative emission rates.

The combined analysis of radiative and RISC rates provides insights into potential molecules as TADF emitters. **CzBPO** and

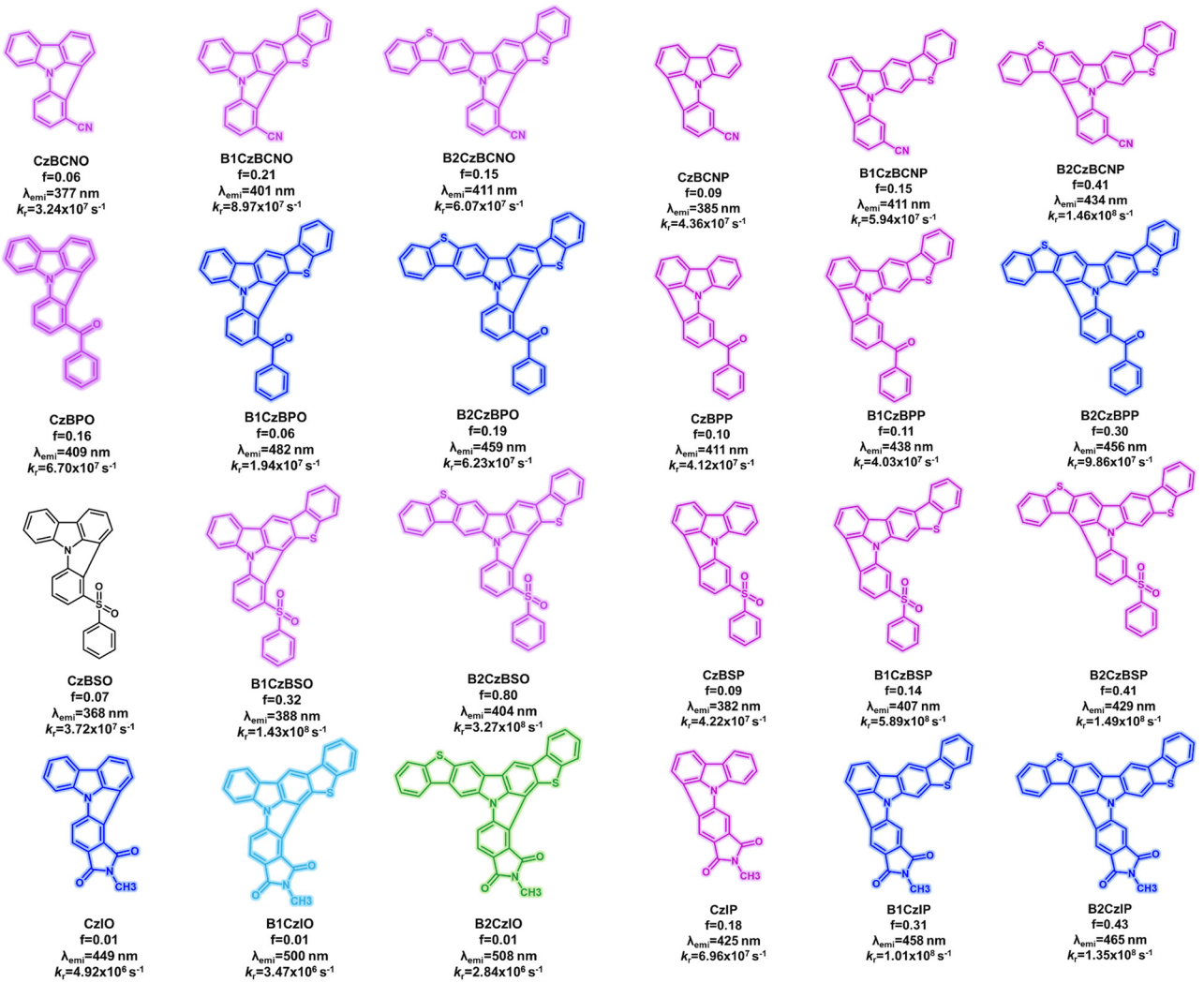

Fig. 5 Pictorial representation of the chemical structures of various molecules considered in this study and their oscillator strength values (*f*), emission values (λ_{emi}), and rate of radiative decay (k_r).

CzIO show much faster k_{RISC} due to strong SOC and smaller ΔE_{ST}, but weaker k_r (6.70×10^7 and 4.63×10^6 s^{-1}) limits the emission efficiency. Molecules such as **B1CzBSO**, **B2CzBSO**, **B1CzIP**, **B2CzBCNP**, **B2CzBSP** and **B2CzIP** exhibited high k_r rates. In particular, **B2CzBSO** combines with a higher k_{RISC} (1.00×10^7 s^{-1}), indicating that this molecule can efficiently up-convert triplet excitons into emissive singlets, making it a potential HLCT emitter compared to experimental molecules **CzIO** and **CzIP**.

5.2. Rate of non-radiative emission (k_{nr})

The rate of non-radiative decay depends on two factors: the Huang–Rhys (HR) factors and the reorganization energy (λ). To more clearly define the nonradiative energy dissipation pathways of the S_1 state, we performed a detailed analysis of the relationship between the HR factor and λ with normal mode frequencies. This analysis provides quantitative data on the nonradiative decay rates in solvents. The HR factor describes the change in vibrational quanta that occurs when the electronic state changes. The following equation was used to calculate the HR factor:

$$HR_i = \frac{\omega_i D_i^2}{2\hbar} \quad (3)$$

In the above equation, ω_i is the vibrational frequency of the ith normal mode, $\hbar$ is the reduced Planck constant and D_i is the displacement for mode i between the equilibrium geometry of two electronic states (S_0 and S_1). A greater HR factor (or stronger vibronic coupling) can lead to higher nonradiative decay rates by enabling nonradiative decay pathways through increased interactions with vibrational modes.

λ_{es} can be calculated using the harmonic oscillator approximation as the sum of the contributions from the normal-mode analysis equation:

$$\lambda_{es} = \sum_{i \in es} \lambda_i = \sum_{i \in es} \hbar \omega_i HR_i \quad (4)$$

where $\hbar$ is the reduced Planck constant, ω_i is the vibrational

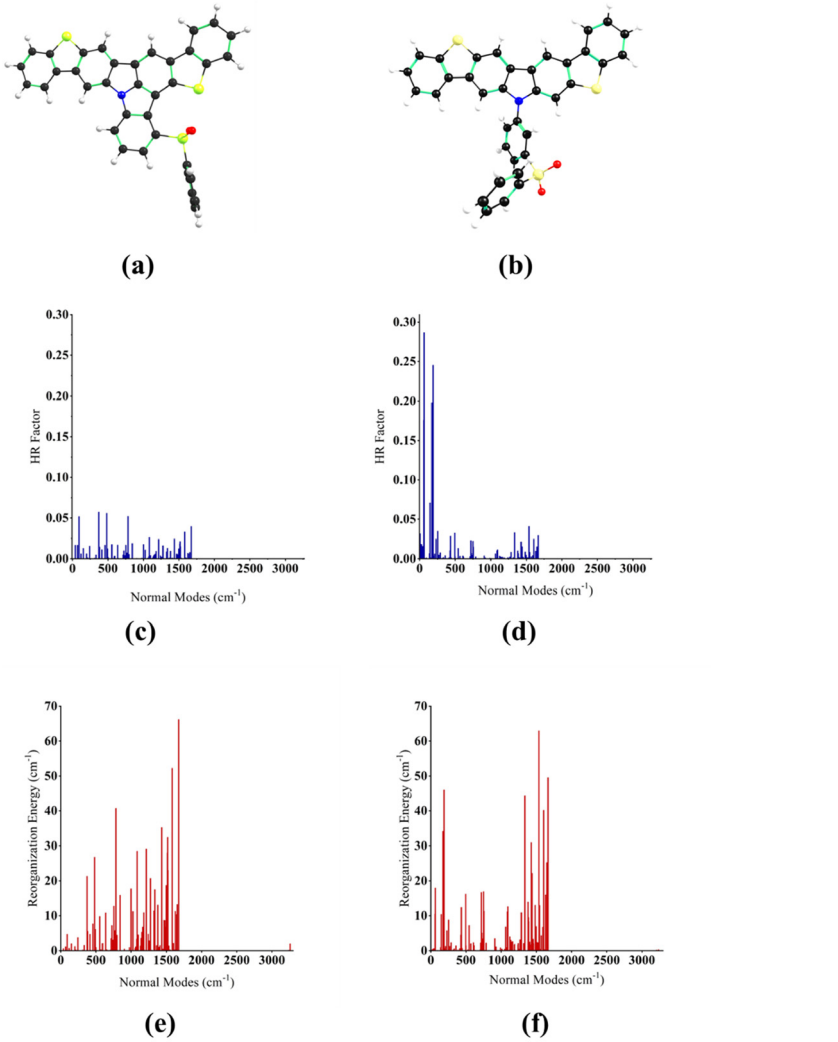

S_1 = 3.08 eV	S_1 = 3.22 eV
RMSD= 0.017 Å	RMSD= 0.054 Å
λ_{es} = 740 cm^{-1}	λ_{es} = 748 cm^{-1}
k_{nr}= 6.50 X 10^8 s^{-1}	k_{nr}= 2.18 X 10^9 s^{-1}
Φ=0.34	Φ =0.01

Fig. 6 Optimized geometries of the (a) rigid (**B2CzBSO**-R) and (b) non-rigid configuration (**B2CzBSO**-NR) of **B2CzBSO**. Calculated HR factors ((c) and (d)) and reorganization energy ((e) and (f)) of the rigid (**B2CzBSO**-R) and non-rigid configurations (**B2CzBSO**-NR), respectively.

frequency of the *i*th normal mode, and HR_i is the HR factor for mode *i* for the first excited state (S_1).

In order to highlight the importance of C–C bond interlocking, we considered two different configurations, *viz.*, (i) **B2CzBSO**-R, which contains the C–C interlocking and represents the rigid structure, and (ii) **B2CzBSO**-NR, a non-interlocked analogue designed to evaluate the effect of structural flexibility. We analysed the Huang–Rhys (HR) factors and reorganization energy for the **B2CzBSO**-R and **B2CzBSO**-NR emitters as a function of the normal mode frequency to gain deeper insight into the vibrational contributions to non-radiative decay pathways (Fig. 6). The results reveal that the rigid **B2CzBSO** (**B2CzBSO**-R) molecule exhibits notably lower HR factors, particularly in the low-frequency region (<500 cm^{-1}). Because the non-radiative decay rate (k_{nr}) is directly proportional to the HR factor, the reduced HR factor in **B2CzBSO**-R correlates with a suppressed k_{nr}. The reduction in k_{nr} enhances the radiative efficiency and maintains high photoluminescence quantum yields (Fig. 6(c)).

To understand the impact of structural rigidity, we considered a nonrigid analog of **B2CzBSO** (**B2CzBSO**-NR, shown in Fig. 6(b)). A comparison of the k_{nr}, HR factors, and reorganization energies will provide insights into the impact of structural rigidity. The non-rigid analogue of **B2CzBSO**-NR displayed a higher HR factor of 0.30 within the same low-frequency range (<500 cm^{-1}), as shown in Fig. 6(d). This increase was

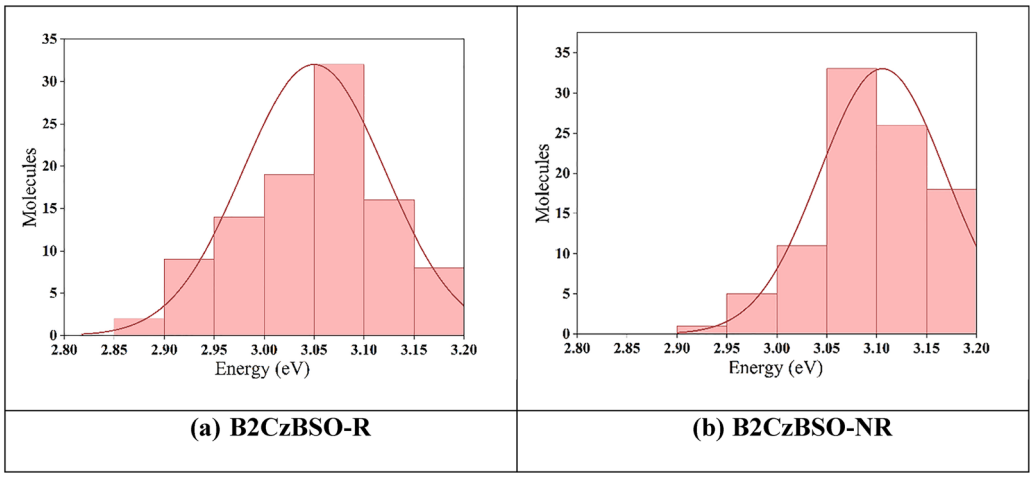

Fig. 7 (a) Distribution of S_1 excitation energies for 100 **B2CzBSO**-R conformers extracted from MD trajectories. (b) Corresponding distribution for **B2CzBSO**-NR. TD-DFT calculations were performed at the PBE0/6-31G(d,p) level on the structures obtained from MD simulations. The **B2CzBSO**-R system exhibits a narrower and more centralized energy profile compared to the broader distribution observed in the **B2CzBSO**-NR counterpart.

attributed to the enhanced structural flexibility during the electronic excitation. These findings reinforce the importance of molecular rigidity in designing efficient HLCT emitters, as lower HR factors help reduce energy loss through nonradiative channels and support narrowband emission profiles critical for high-performance optoelectronic applications.

5.3. Distribution of S_1 energy

A detailed description of the atomistic molecular dynamic simulation is provided in the SI. The resulting distributions of S_1 energies are depicted in Fig. 7(a) and (b) for the rigid and non-rigid systems of **B2CzBSO**, respectively.

In the case of the non-rigid **B2CzBSO**-NR, the S_1 energies are broadly distributed, with a mean value of 3.04 eV and a standard deviation of $\pm$0.06 eV. Notably, approximately 32% of the sampled conformers exhibited excitation energies in the range of 2.9–3.2 eV, indicating significant conformational flexibility and energetic dispersion.

Conversely, the rigid **B2CzBSO**-R molecules exhibited a narrower distribution centred around 2.94 eV with a standard deviation of $\pm$0.122 eV. The majority of conformers (nearly all) were clustered within a more confined energy window of 2.9–3.1 eV, reflecting a more homogeneous conformational landscape and reduced structural dynamics. These results highlight the influence of molecular rigidity on the photophysical behaviour of **B2CzBSO**, where structural constraints in the rigid derivative led to narrower S_1 energy distributions, potentially favouring more consistent optical and electronic properties that are desirable for device applications.

6. Conclusion

In this study, we systematically designed and computationally analysed a series of 24 hybrid local and charge transfer (HLCT) emitters by systematically varying the strengths of the donor and acceptor units and interlocking patterns. Geometrical, electronic, excited-state properties are evaluated on these molecules to elucidate the role of backbone rigidification in modulating the excited state dynamics. The designed molecules consisted of *ortho*- and *para*-interlocked configurations constructed using three donor moieties (carbazole (Cz), mono benzo thiophene carbazole (B1Cz), and dibenzo thiophene carbazole (B2Cz)) in combination with four distinct acceptors: cyano benzene (BCN), benzophenone (BP), sulfonyl dibenzene (BS), and *n*-methyl phthalimide (I). We established a structure–property relationship linking interlocking geometry, excited-state character, radiative, and non-radiative decay properties.

We found that the *ortho*-interlocked structures exhibited smaller ΔE_{ST} values owing to the increased charge-transfer character and spatial separation of the Frontier molecular orbitals. In addition to ΔE_{ST}, spin–orbit coupling (SOC) values were analysed, as they play a crucial role in promoting RISC from higher-lying triplet states. Furthermore, the interlocking strategy improved the overlap between the HOMO and the LUMO. As a result, high oscillator strength (f) values were observed for the newly designed molecules. Among all the designed molecules, the **B2CzBSO** emitter exhibited a favourable balance of small ΔE_{ST}, enhanced SOC, efficient RISC, and strong oscillator strength, identifying it as a promising candidate.

Comparison between rigid **B2CzBSO** (**B2CzBSO**-R) and non-rigid analogues of **B2CzBSO** (**B2CzBSO**-NR) reveals that C–C interlocking reduces the low-frequency vibrational contributions and HR factors, thereby suppressing the non-radiative decay pathways. Although most of the properties are similar in the rigid and non-rigid structures, we noted that backbone interlocking can simultaneously maintain radiative efficiency and suppress the non-radiative pathways in this structural class. Overall, this study establishes structural interlocking as an effective molecular-design strategy for achieving balanced radiative and non-radiative decay processes.

Conflicts of interest

The authors declare no competing financial interests.

Data availability

The data supporting this article have been included as part of the supplementary information (SI). The supplementary information includes additional details on comparison of performance of various DFT functionals, HOMO and LUMO wavefunctions, NTOs. See DOI: https://doi.org/10.1039/d5ma01318f.

Acknowledgements

L. N. S. L. P. thanks SRM University-AP for the junior research fellowship. M. K. R. also thanks SRM University-AP, Andhra Pradesh, for providing the central computational facility.

References

1 C. W. Tang and S. A. VanSlyke, Organic electroluminescent diodes, *Appl. Phys. Lett.*, 1987, **51**, 913–915.
2 M. A. Baldo, D. F. O'Brien, M. E. Thompson and S. R. Forrest, Excitonic singlet-triplet ratio in a semiconducting organic thin film, *Phys. Rev. B: Condens. Matter Mater. Phys.*, 1999, **60**, 14422–14428.
3 M. A. Baldo, D. F. O'Brien, Y. You, A. Shoustikov, S. Sibley, M. E. Thompson and S. R. Forrest, Highly efficient phosphorescent emission from organic electroluminescent devices, *Nature*, 1998, **395**, 151–154.
4 D. Zhang, T. Huang and L. Duan, Emerging Self-Emissive Technologies for Flexible Displays, *Adv. Mater.*, 2020, **32**, 1902391.
5 R. H. Friend, R. W. Gymer, A. B. Holmes, J. H. Burroughes, R. N. Marks, C. Taliani, D. D. C. Bradley, D. A. D. Santos, J. L. Brédas, M. Lögdlund and W. R. Salaneck, Electroluminescence in conjugated polymers, *Nature*, 1999, **397**, 121–128.
6 J. Huang, J.-H. Su and H. Tian, The development of anthracene derivatives for organic light-emitting diodes, *J. Mater. Chem.*, 2012, **22**, 10977.
7 J. Eng and T. J. Penfold, Understanding and Designing Thermally Activated Delayed Fluorescence Emitters: Beyond the Energy Gap Approximation, *Chem. Rec.*, 2020, **20**, 831–856.
8 T. Chen, L. Zheng, J. Yuan, Z. An, R. Chen, Y. Tao, H. Li, X. Xie and W. Huang, Understanding the Control of Singlet-Triplet Splitting for Organic Exciton Manipulating: A Combined Theoretical and Experimental Approach, *Sci. Rep.*, 2015, **5**, 10923.
9 Q. Zhang, H. Kuwabara, W. J. Potscavage, S. Huang, Y. Hatae, T. Shibata and C. Adachi, Anthraquinone-Based Intramolecular Charge-Transfer Compounds: Computational Molecular Design, Thermally Activated Delayed Fluorescence, and Highly Efficient Red Electroluminescence, *J. Am. Chem. Soc.*, 2014, **136**, 18070–18081.
10 A. Monkman, Why Do We Still Need a Stable Long Lifetime Deep Blue OLED Emitter?, *ACS Appl. Mater. Interfaces*, 2022, **14**, 20463–20467.
11 C. Rothe and A. P. Monkman, Triplet exciton migration in a conjugated polyfluorene, *Phys. Rev. B: Condens. Matter Mater. Phys.*, 2003, **68**, 075208.
12 C.-J. Chiang, A. Kimyonok, M. K. Etherington, G. C. Griffiths, V. Jankus, F. Turksoy and A. P. Monkman, Ultrahigh Efficiency Fluorescent Single and Bi-Layer Organic Light Emitting Diodes: The Key Role of Triplet Fusion, *Adv. Funct. Mater.*, 2013, **23**, 739–746.
13 S. Xiao, Y. Gao, R. Wang, H. Liu, W. Li, C. Zhou, S. Xue, S.-T. Zhang, B. Yang and Y. Ma, Highly efficient hybridized local and Charge-transfer (HLCT) Deep-blue electroluminescence with excellent molecular horizontal orientation, *Chem. Eng. J.*, 2022, **440**, 135911.
14 D. Cui, L. Zhang, J. Zhang, W. Li, J. Chen, Z. Guo, C. Sun, Y. Wang, W. Wang, S. Li, W. Huang, C. Zheng and R. Chen, Hybrid Local and Charge-Transfer Material with Ultralong Room Temperature Phosphorescence for Efficient Organic Afterglow Light-Emitting Diodes, *Angew. Chem., Int. Ed.*, 2024, **63**, e202411588.
15 X. Hong, D. Zhang, C. Yin, Q. Wang, Y. Zhang, T. Huang, J. Wei, X. Zeng, G. Meng, X. Wang, G. Li, D. Yang, D. Ma and L. Duan, TADF molecules with π-extended acceptors for simplified high-efficiency blue and white organic light-emitting diodes, *Chem*, 2022, **8**, 1705–1719.
16 T. Nakagawa, S.-Y. Ku, K.-T. Wong and C. Adachi, Electroluminescence based on thermally activated delayed fluorescence generated by a spirobifluorene donor–acceptor structure, *Chem. Commun.*, 2012, **48**, 9580.
17 Y. Zhang, X. Liang, X. Luo, S. Song, S. Li, Y. Wang, Z. Mao, W. Xu, Y. Zheng, J. Zuo and Y. Pan, Chiral Spiro-Axis Induced Blue Thermally Activated Delayed Fluorescence Material for Efficient Circularly Polarized OLEDs with Low Efficiency Roll-Off, *Angew. Chem. Int. Ed.*, 2021, **60**, 8435–8440.
18 H. Bässler and B. Schweitzer, Site-Selective Fluorescence Spectroscopy of Conjugated Polymers and Oligomers, *Acc. Chem. Res.*, 1999, **32**, 173–182.
19 D. J. Stewart, M. J. Dalton, S. L. Long, R. Kannan, Z. Yu, T. M. Cooper, J. E. Haley and L.-S. Tan, Steric hindrance inhibits excited-state relaxation and lowers the extent of intramolecular charge transfer in two-photon absorbing dyes, *Phys. Chem. Chem. Phys.*, 2016, **18**, 5587–5596.
20 X. Liu, Z. Chen, C. Zheng, M. Chen, W. Liu, X. Zhang and C. Lee, Nearly 100% Triplet Harvesting in Conventional Fluorescent Dopant-Based Organic Light-Emitting Devices Through Energy Transfer from Exciplex, *Adv. Mater.*, 2015, **27**, 2025–2030.
21 S. Youn Lee, T. Yasuda, H. Nomura and C. Adachi, High-efficiency organic light-emitting diodes utilizing thermally activated delayed fluorescence from triazine-based donor–acceptor hybrid molecules, *Appl. Phys. Lett.*, 2012, **101**, 093306.

22 Q. Zhang, B. Li, S. Huang, H. Nomura, H. Tanaka and C. Adachi, Efficient blue organic light-emitting diodes employing thermally activated delayed fluorescence, *Nat. Photon.*, 2014, **8**, 326–332.
23 J. Lee, K. Shizu, H. Tanaka, H. Nomura, T. Yasuda and C. Adachi, Oxadiazole- and triazole-based highly-efficient thermally activated delayed fluorescence emitters for organic light-emitting diodes, *J. Mater. Chem. C*, 2013, **1**, 4599.
24 T. Hatakeyama, K. Shiren, K. Nakajima, S. Nomura, S. Nakatsuka, K. Kinoshita, J. Ni, Y. Ono and T. Ikuta, Ultrapure Blue Thermally Activated Delayed Fluorescence Molecules: Efficient HOMO–LUMO Separation by the Multiple Resonance Effect, *Adv. Mater.*, 2016, **28**, 2777–2781.
25 M. Liu, X. Li, D. C. Chen, Z. Xie, X. Cai, G. Xie, K. Liu, J. Tang, S. Su and Y. Cao, Study of Configuration Differentia and Highly Efficient, Deep-Blue, Organic Light-Emitting Diodes Based on Novel Naphtho[1,2-*d*]imidazole Derivatives, *Adv. Funct. Mater.*, 2015, **25**, 5190–5198.
26 J. W. Sun, J. Y. Baek, K.-H. Kim, C.-K. Moon, J.-H. Lee, S.-K. Kwon, Y.-H. Kim and J.-J. Kim, Thermally Activated Delayed Fluorescence from Azasiline Based Intramolecular Charge-Transfer Emitter (DTPDDA) and a Highly Efficient Blue Light Emitting Diode, *Chem. Mater.*, 2015, **27**, 6675–6681.
27 J. Zhang, D. Ding, Y. Wei, F. Han, H. Xu and W. Huang, Multiphosphine-Oxide Hosts for Ultralow-Voltage-Driven True-Blue Thermally Activated Delayed Fluorescence Diodes with External Quantum Efficiency beyond 20%, *Adv. Mater.*, 2016, **28**, 479–485.
28 D.-Y. Chen, W. Liu, C.-J. Zheng, K. Wang, F. Li, S. Tao, X.-M. Ou and X.-H. Zhang, Isomeric Thermally Activated Delayed Fluorescence Emitters for Color Purity-Improved Emission in Organic Light-Emitting Devices, *ACS Appl. Mater. Interfaces*, 2016, **8**, 16791–16798.
29 R. Ansari, W. Shao, S.-J. Yoon, J. Kim and J. Kieffer, Charge Transfer as the Key Parameter Affecting the Color Purity of Thermally Activated Delayed Fluorescence Emitters, *ACS Appl. Mater. Interfaces*, 2021, **13**, 28529–28537.
30 A. Kumar, P. Keerthika, S. W. Han, J. Y. Lee and R. K. Konidena, One Shift, Huge Impact: Isomeric Engineering Unlocks Pure Organic Ultra-Narrowband Dual Functional Ultraviolet Emitters for High-Performance OLEDs, *ACS Mater. Lett.*, 2026, **8**, 544–550.
31 S. Kothavale, R. K. Konidena, H. Lee and J. Y. Lee, Stepwise Emission Tuning of Thermally Activated Delayed Fluorescence Emitters from the Orange to Near-Infrared Region by Rational Molecular Design, *Org. Lett.*, 2025, **27**, 12933–12938.
32 A. Kumar, S. Han, D. Kumar Sharma, J. Yeob Lee and R. Kumar Konidena, A streamlined steric-shielding approach toward efficient narrowband (FWHM $\sim$ 18 nm) ultra-violet emitters for OLEDs, *Chem. Commun.*, 2025, **61**, 18116–18119.
33 H. Uoyama, K. Goushi, K. Shizu, H. Nomura and C. Adachi, Highly efficient organic light-emitting diodes from delayed fluorescence, *Nature*, 2012, **492**, 234–238.
34 F. B. Dias, J. Santos, D. R. Graves, P. Data, R. S. Nobuyasu, M. A. Fox, A. S. Batsanov, T. Palmeira, M. N. Berberan-Santos, M. R. Bryce and A. P. Monkman, The Role of Local Triplet Excited States and D-A Relative Orientation in Thermally Activated Delayed Fluorescence: Photophysics and Devices, *Adv. Sci.*, 2016, 1600080.
35 T. Hatakeyama, K. Shiren, K. Nakajima, S. Nomura, S. Nakatsuka, K. Kinoshita, J. Ni, Y. Ono and T. Ikuta, Ultrapure Blue Thermally Activated Delayed Fluorescence Molecules: Efficient HOMO–LUMO Separation by the Multiple Resonance Effect, *Adv. Mater.*, 2016, **28**, 2777–2781.
36 X.-F. Luo, X. Xiao and Y.-X. Zheng, Recent progress in multi-resonance thermally activated delayed fluorescence emitters with an efficient reverse intersystem crossing process, *Chem. Commun.*, 2024, **60**, 1089–1099.
37 C.-Y. Chan, L.-S. Cui, J. U. Kim, H. Nakanotani and C. Adachi, Rational Molecular Design for Deep-Blue Thermally Activated Delayed Fluorescence Emitters, *Adv. Funct. Mater.*, 2018, **28**, 1706023.
38 V. V. Patil, W. P. Hong and J. Y. Lee, Indolocarbazole Derivatives for Highly Efficient Organic Light-Emitting Diodes, *Adv. Energy Mater.*, 2025, **15**, 2400258.
39 X. Wang, L. Duan and D. Zhang, Indolocarbazole-Based Multiple-Resonance Molecules: an Emerging Class of Full-Color, Narrowband Emitters for Organic Light-Emitting Diodes, *Chem. – Eur. J.*, 2023, **29**, e202300701.
40 V. V. Patil, J. Lim and J. Y. Lee, Strategic Synchronization of 7,7-Dimethyl-5,7-dihydroindeno[2,1-*b*]carbazole for Narrow-Band, Pure Violet Organic Light-Emitting Diodes with an Efficiency of $>$ 5% and a CIE y Coordinate of $<$ 0.03, *ACS Appl. Mater. Interfaces*, 2021, **13**, 14440–14446.
41 H. Sun, C. Zhong and J.-L. Brédas, Reliable Prediction with Tuned Range-Separated Functionals of the Singlet–Triplet Gap in Organic Emitters for Thermally Activated Delayed Fluorescence, *J. Chem. Theory Comput.*, 2015, **11**, 3851–3858.
42 W. J. Hehre, R. Ditchfield and J. A. Pople, Self—Consistent Molecular Orbital Methods. XII. Further Extensions of Gaussian—Type Basis Sets for Use in Molecular Orbital Studies of Organic Molecules, *J. Chem. Phys.*, 1972, **56**, 2257–2261.
43 J. Schirmer, Review of the foundations of time-dependent density-functional theory (TDDFT), *Phys. Chem. Chem. Phys.*, 2025, **27**, 4992–5005.
44 R. L. Martin, Natural transition orbitals, *J. Chem. Phys.*, 2003, **118**, 4775–4777.
45 S. Kumar, L. G. Franca, K. Stavrou, E. Crovini, D. B. Cordes, A. M. Z. Slawin, A. P. Monkman and E. Zysman-Colman, Investigation of Intramolecular Through-Space Charge-Transfer States in Donor–Acceptor Charge-Transfer Systems, *J. Phys. Chem. Lett.*, 2021, **12**, 2820–2830.
46 M. J. Frisch, G. W. Trucks, H. B. Schlegel, G. E. Scuseria, M. A. Robb, J. R. Cheeseman, G. Scalmani, V. Barone, G. A. Petersson, H. Nakatsuji, X. Li, M. Caricato, A. V. Marenich, J. Bloino, B. G. Janesko, R. Gomperts, B. Mennucci, H. P. Hratchian, J. V. Ortiz, A. F. Izmaylov, J. L. Sonnenberg, D. Williams-Young, F. Ding, F. Lipparini, F. Egidi, J. Goings,

B. Peng, A. Petrone, T. Henderson, D. Ranasinghe, V. G. Zakrzewski, J. Gao, N. Rega, G. Zheng, W. Liang, M. Hada, M. Ehara, K. Toyota, R. Fukuda, J. Hasegawa, M. Ishida, T. Nakajima, Y. Honda, O. Kitao, H. Nakai, T. Vreven, K. Throssell, J. A. Montgomery Jr., J. E. Peralta, F. Ogliaro, M. J. Bearpark, J. J. Heyd, E. N. Brothers, K. N. Kudin, V. N. Staroverov, T. A. Keith, R. Kobayashi, J. Normand, K. Raghavachari, A. P. Rendell, J. C. Burant, S. S. Iyengar, J. Tomasi, M. Cossi, J. M. Millam, M. Klene, C. Adamo, R. Cammi, J. W. Ochterski, R. L. Martin, K. Morokuma, O. Farkas, J. B. Foresman and D. J. Fox, 2016.

47 F. Neese, F. Wennmohs, U. Becker and C. Riplinger, The ORCA quantum chemistry program package, *J. Chem. Phys.*, 2020, **152**, 224108.

48 P. K. Samanta, D. Kim, V. Coropceanu and J.-L. Brédas, Up-Conversion Intersystem Crossing Rates in Organic Emitters for Thermally Activated Delayed Fluorescence: Impact of the Nature of Singlet *vs*. Triplet Excited States, *J. Am. Chem. Soc.*, 2017, **139**, 4042–4051.

49 S. Kuila, H. Miranda-Salinas, J. Eng, C. Li, M. R. Bryce, T. J. Penfold and A. P. Monkman, Rigid and planar π-conjugated molecules leading to long-lived intramolecular charge-transfer states exhibiting thermally activated delayed fluorescence, *Nat. Commun.*, 2024, **15**, 9611.

50 T. Liu, X. Chen, J. Zhao, W. Wei, Z. Mao, W. Wu, S. Jiao, Y. Liu, Z. Yang and Z. Chi, Hybridized local and charge-transfer excited state fluorophores enabling organic light-emitting diodes with record high efficiencies close to 20%, *Chem. Sci.*, 2021, **12**, 5171–5176.

51 C. Zhou, S. Xiao, M. Wang, W. Jiang, H. Liu, S. Zhang and B. Yang, Modulation of Excited State Property Based on Benzo[a, c]phenazine Acceptor: Three Typical Excited States and Electroluminescence Performance, *Front Chem.*, 2019, **7**, 141.

52 X.-K. Chen, D. Kim and J.-L. Brédas, Thermally Activated Delayed Fluorescence (TADF) Path toward Efficient Electroluminescence in Purely Organic Materials: Molecular Level Insight, *Acc. Chem. Res.*, 2018, **51**, 2215–2224.